Lateral-Torsional Buckling Research Needs and Validation of an Experimental Setup in the Elastic Range

RYAN SLEIN, JOSHUA S. BUTH, WAJAHAT LATIF, AJIT M. KAMATH, AMMAR A. ALSHANNAQ, RYAN J. SHERMAN, DAVID W. SCOTT, and DONALD W. WHITE

ABSTRACT

The AISC *Specification* Chapter F I-section member flexural resistance equations are a central part of structural steel design in the United States. The provisions of Sections F4 and F5 address general singly and doubly symmetric I-section members. Analytical studies and experimental tests subsequent to the implementation of these provisions within the 2005 AISC *Specification* suggest that the corresponding inelastic lateral-torsional buckling (LTB) and tension flange yielding (TFY) resistance equations can be improved, resulting in significantly larger predicted strengths in certain cases and somewhat smaller predicted strengths in other cases. Additional large-scale experimental tests, specifically pushing into the inelastic LTB range, need to be conducted to further investigate these predictions. The broad objective of the additional tests is to achieve a target reliability index of $\beta = 2.6$ for building design at a live-to-dead load ratio of 3.0 throughout the design space involving all types of statically determinate I-section flexural members.

This paper discusses the need for these tests, specifically focusing on the details of how the test fixtures and bracing systems were configured to minimize incidental restraint, which is a critical consideration when conducting flexural experimental testing. The paper discusses the validation of the testing system by comparison of elastic buckling experimental results to analytical and numerical solutions.

Keywords: lateral-torsional buckling, experimental testing, incidental restraint.

INTRODUCTION

The Chapter F equations in the AISC *Specification for Structural Steel Buildings*, hereafter referred to as the AISC *Specification* (AISC, 2016b), provide a broad characterization of the flexural resistance of all types of I-section members, including rolled and welded members; members with doubly and singly symmetric cross-section profiles; and members with compact, noncompact, or slender flanges and/or webs, failing by plastic, inelastic, or elastic lateral-torsional buckling (LTB). Closely related equations exist within the *AASHTO LRFD Bridge Design Specifications* (AASHTO, 2020).

Relatively comprehensive assessments of analytical studies and experimental test results conducted to date have raised concerns that AISC *Specification* Sections F4 and F5 flexural resistance provisions may not satisfy accepted target reliability indices in certain cases pertaining to the LTB of I-section members (Subramanian et al., 2018; Subramanian and White, 2017). However, the experimental test data are quite sparse within a number of "regions" of the corresponding design space. Additionally, AISC *Specification* Sections F4 and F5 can be enhanced by eliminating the current tension flange yielding (TFY) limit state provisions. Allowing for development of significant reserve capacity involving yielding in flexural tension by incorporating early tension yielding effects into the calculation of the cross-section yield moment to the compression flange, M_{yc} (Toğay and White, 2018).

Quality experimental data is critical for the validation of refined shell finite element analysis (FEA) procedures that can be employed to investigate the flexural resistances within the design space more comprehensively.

This paper focuses on the validation of the testing configuration used to conduct inelastic tests to achieve the above objectives. Lateral-torsional buckling experimental

Ryan Slein, Graduate Research Assistant, Georgia Institute of Technology, Atlanta, Ga. Email: ryan.slein@gatech.edu (corresponding)

Joshua S. Buth, Civil Engineer II, Georgia Department of Transportation, Atlanta Ga. Email: JButh@dot.ga.gov

Wajahat Latif, Graduate Research Assistant, Georgia Institute of Technology, Atlanta, Ga. Email: wlatif@gatech.edu

Ajit M. Kamath, Graduate Research Assistant, Georgia Institute of Technology, Atlanta, Ga. Email: ajit.kamath@gatech.edu

Ammar A. Alshannaq, Graduate Research Assistant, Georgia Institute of Technology, Atlanta, Ga. Email: aalshannaq@gatech.edu

Ryan J. Sherman, Assistant Professor, Georgia Institute of Technology, Atlanta, Ga. Email: ryan.sherman@ce.gatech.edu

David W. Scott, Professor and Chair, Department of Civil Engineering and Construction., Georgia Southern University, Statesboro, Ga. Email: dscott@georgiasouthern.edu

Donald W. White, Professor, Georgia Institute of Technology, Atlanta, Ga. Email: dwhite@ce.gatech.edu

Paper No. 2020-12

results can be sensitive to incidental restraint in the testing configuration (Ziemian, 2010). The testing configuration described in this paper utilizes polytetrafluoroethylene-(PTFE-) coated spherical bearings for multi-rotational degree-of-freedom releases, mechanical bearings for the single rotational degree-of-freedom releases (as part of a Watt's linkage bracing system), and lubricated roller packs for single translational degree-of-freedom releases. The effectiveness of these "releases" of rotational and translational constraints is evaluated directly by testing a specimen in the elastic LTB range and comparing the measured responses to various analytical and numerical solutions.

TEST CONFIGURATION

The experimental test setup was designed to minimize incidental restraint and remove load-height effects. Incidental restraint can have a measurable impact on large-scale experimental LTB beam results by increasing the capacity beyond that based on the ideal boundary conditions (Ziemian, 2010). The test configuration was designed to fully release or fix selected degrees-of-freedom at the bearing, load, and bracing points. Load-height effects at the load points can make the calibration of design equations to observed specimen behavior more complex. To eliminate load-height effects, the lateral and torsional displacements were restrained at the bearing and load points in all the experiments conducted in this research. The design of the test setup involved an extension of the concepts discussed in the Structural Stability Research Council (SSRC) Technical Memorandum No. 9 on flexural testing (Ziemian, 2010).

Figure 1 provides an elevation view of a test specimen, discussed throughout this paper, under three-point bending. The elevation view and measured section dimensions in Figure 1 are drawn to scale and show instrumentation locations and the corresponding moment diagram.

Figure 2 is a photograph of the test specimen within testing frame. The white member is the test specimen, the blue members are the bracing reaction system, and the gray members are the load frame. The loading and support fixtures and bracing details are discussed in the following sections.

Load and Bearing Fixtures

Roller boundary conditions were provided at the bearing locations. The overall boundary conditions were symmetric about the mid-length of the test specimens. Longitudinal translation was permitted via a lubricated roller pack composed of four 2.5-in.-diameter solid steel rods. A 100-kip load cell was located above each roller pack. Transverse displacement was restrained at the bearing locations via Watt's linkage braces discussed in the following section. The three rotational degrees-of-freedom at the supports were released via PTFE-lined spherical thrust bearings. The PTFE thrust bearings allowed free in-plane rotation due to the major-axis bending of the specimens and free out-of-plane rotation associated with flange warping and/or lateral bending. The spherical bearing was seated in a counter-bored plate on top of the load cell. Weld beads were placed on the flange of the specimen to securely seat the opposite side of the spherical bearing on the specimen. Figure 3 provides a conceptual drawing of the bearing detail used for all tests as well as a photograph of the final bearing detail prior to placing the spherical thrust bearing at the top.

In addition, a PTFE spherical thrust bearing was located at the point of load application (e.g., at the midspan of the three-point bending test specimens). Load-point bracing was provided via a Watt's linkage system. Figure 4 shows the conceptual and implemented boundary condition at the point of load application.

Bracing

The bracing system was designed using a mechanical system known as a Watt's linkage. The Watt's linkage restrains displacement perpendicular to the girder web, while allowing

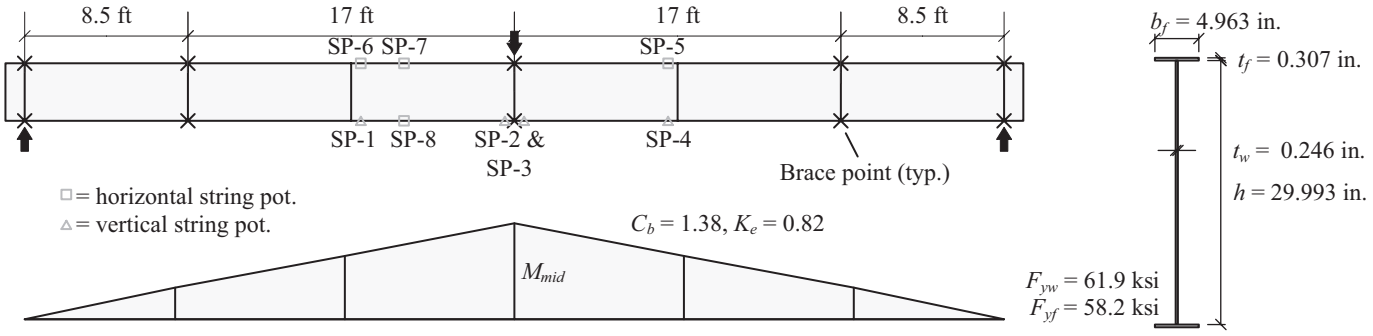

Fig. 1. South-facing elevation view of the elastic test specimen showing the instrumentation locations, corresponding moment diagram, measured section dimensions and properties, and key design parameters C_b *and* K_e.

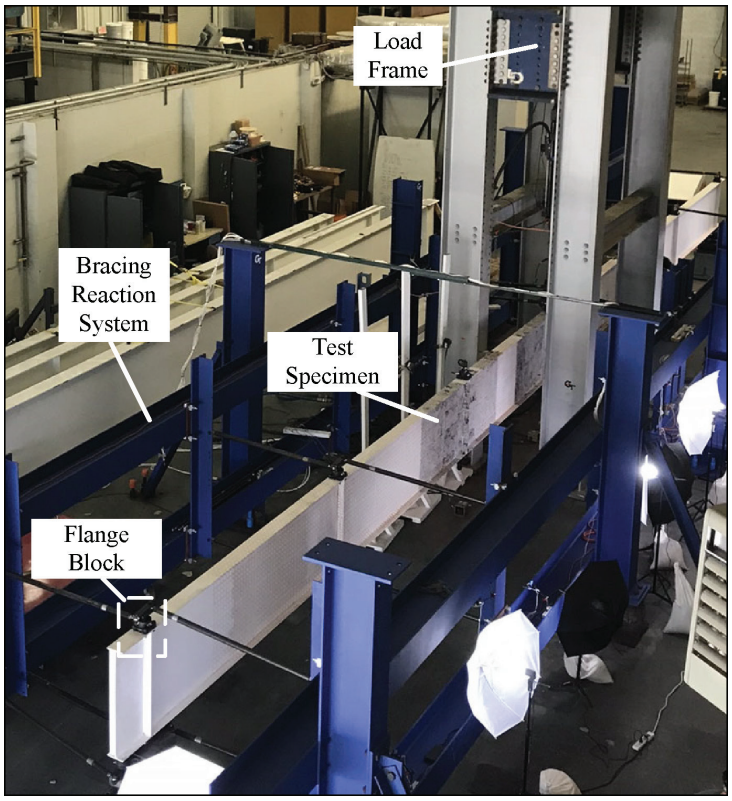

Fig. 2. Perspective view of the test configuration.

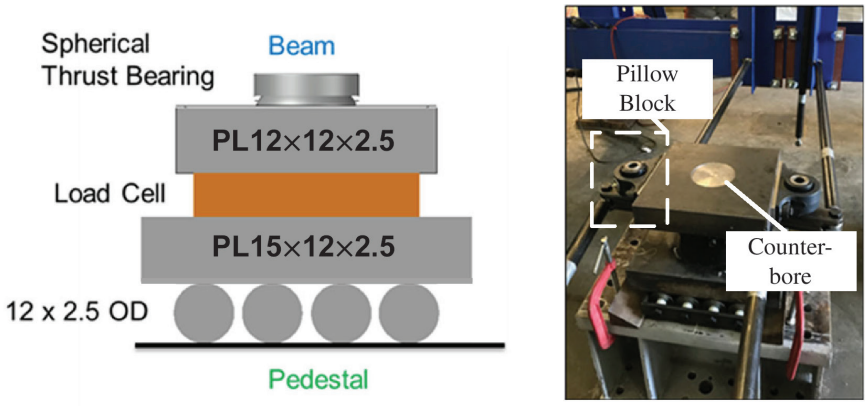

Fig. 3. Bearing boundary condition detail: schematic (left) and implementation (right). The spherical bearing was excluded in the photo to show the counter-bore. The roller pack was chocked in the photo to prevent incidental movement during installation of the test specimen.

free translation in the longitudinal and vertical directions. Watt's linkage bracing has been used previously by Yarimci et al. (1967), Smith et al. (2013), and others. For the current study, the system was comprised of two 4-ft-long tie rods with ball joint rod ends attached to the stiff reaction frames (painted blue in Figure 2) and a 6.5-in.-long center link. The center link is free to rotate about a vertical axis and transfers lateral forces to the girder through a cylindrical mechanical bearing referred to as a flange block. The center link is attached at its mid-length to a pillow block on each side of the 2.5-in.-thick plate containing the counterbore at the load and support points and to a flange block at the other brace points. Figure 5 illustrates the ability of the linkage system to prevent deflections in the direction perpendicular to the girder webs (i.e., the horizontal direction in the figure) under large longitudinal displacements (i.e., displacements in the vertical direction in the figure). In addition, girder vertical deflections (i.e., deflections into and out of the page in the figure) are accommodated by the rotation of the center link about a vertical axis.

The Watt's linkage system does an excellent job of releasing incidental constraint. Annotated photos describing the system are provided in Figure 6 and 7. Several additional unique features added to the design of the bracing system include the following:

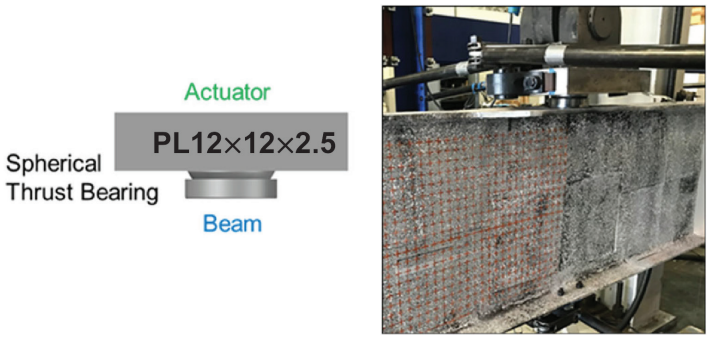

Fig. 4. Load point boundary condition detail: schematic (left) and implementation (right).

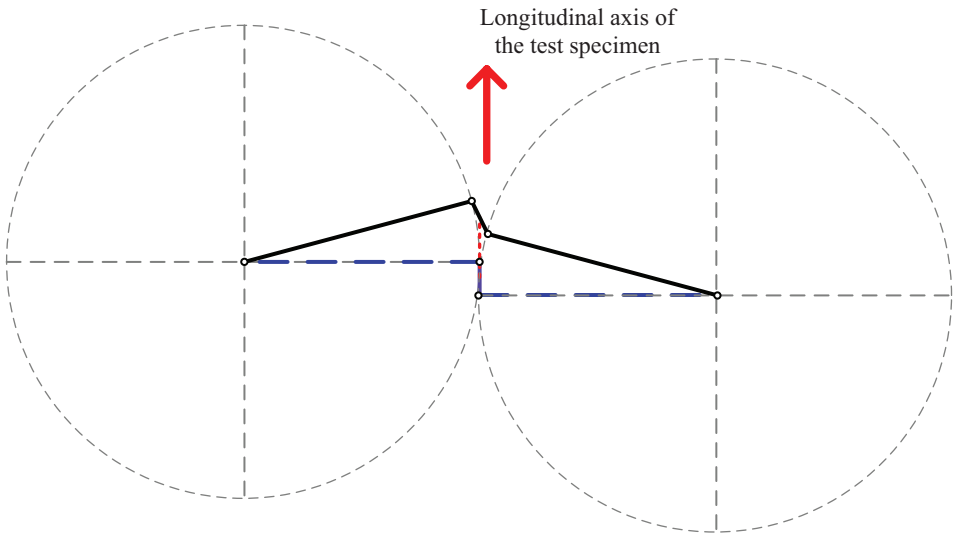

Fig. 5. Plan view illustration of a Watt's linkage movement under a large deflection along the axis of the test specimen. The heavy dashed blue lines represent the initial geometry of the linkage, the solid black lines represent a deformed geometry of the linkage, and the red dashed line illustrates the path of the brace point (i.e., the middle of the center link) between the two geometries.

- Each end of the tie rods was threaded—left-hand threads on one end and right-hand threads on the other. The opposing threads allowed for quick length adjustments via rotation of the rod about its axis, without having to unbolt the ends, allowing for fine adjustments to ensure the test specimen was plumb at each brace point.
- Jam nuts were used to ensure the tie rod length did not change during the loading of the test specimens.
- A rail system was implemented for rapid reconfiguration between different unbraced lengths and bracing configurations. The tie rods were bolted to vertical WT members containing a series of holes accommodating varying specimen heights. The bracing reaction frame was composed of wide flange rails that extended the entire length of the test setup. Friction-based connections by Lindapter (2019) were used to connect the vertical WT sections to the wide flange rails. Each WT slid along the rails to accommodate a range of specimen unbraced lengths.
- Each brace point, including the Lindapter friction-based connection, was designed to accommodate a transverse force of 20 kips. A flange block (a housed cylindrical bearing) was used to release the rotation about the vertical axis at the girder flanges for the Watt's linkage system. At the load application and bearing locations, pillow blocks, with a different housing but the same internal cylindrical bearing, were selected. To prevent pull-out, the outside diameter of the stem connecting the center link to the pillow block was match-machined to the inside diameter of the bearing for a press-fit connection. Additionally, four set screws bear on flats on the center-link stem.

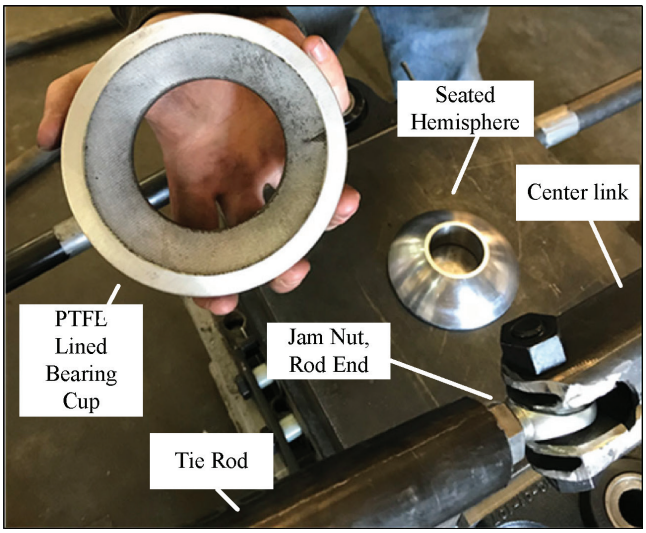

Fig. 6. Components of the boundary conditions.

NUMERICAL MODELING

Finite element methods can predict incipient buckling (bifurcation) by calculating the lowest eigenvalue using the equation

$$\left[K_{e.ff}\right]\left\{\Delta_f\right\} = \lambda\left[-K_{g.ff}\right]\left\{\Delta_f\right\} \quad (1)$$

where $K_{e.ff}$ is the elastic stiffness matrix only considering free degrees of freedom, $K_{g.ff}$ is the geometric stiffness matrix calculated from element forces (or stresses) from a linear elastic analysis for a known reference load P_{ref}, Δ_f is the displacement vector associated with the free degrees of freedom, and λ is the lowest eigenvalue representing the ratio of the elastic critical load to P_{ref} (McGuire et al., 2000).

Iterating P_{ref} until λ goes to 1.0 results in a predicted elastic linear buckling strength. For the test specimens, self-weight and the weight of the bracing components are a constant value, so it is inappropriate to scale a constant reference applied load, P_{ref}, solely by λ. That is, the loading on the system includes a constant load due to the initial self-weight of the specimen and bracing attachments to the specimen, plus the reference load multiplied by the applied load parameter, λ. Once the initial load due to the self-weight is established, then either P_{ref} can be varied and an eigenvalue solution sought such that $\lambda = 1.0$, or a constant applied reference load can be specified and an eigenvalue multiple of this reference load sought corresponding to the buckling of the specimen. In either case, the internal forces are the sum of the constant forces due to the initial

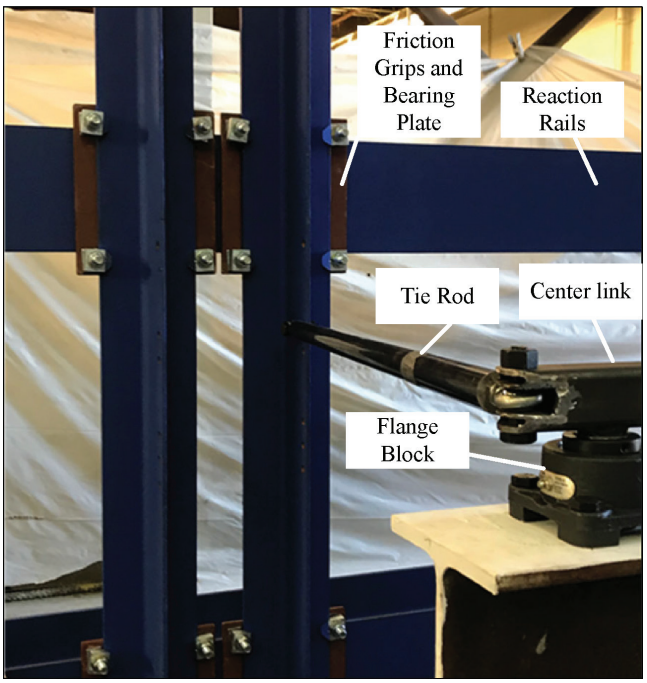

Fig. 7. Components of the bracing system.

self-weight plus the forces due to the additional applied load at buckling. In this research, these elastic buckling calculations were conducted using the finite element software system SABRE2 (White et al., 2020) based on thin-walled open-section (TWOS) beam theory considering warping torsion.

The elastic effective length factor, K_e, is back-calculated by equating the maximum internal moment within the critical unbraced length, at the elastic buckling load level determined by the computational solution, to the equation for the elastic critical moment, M_{cr}, from recommended and AISC *Specification* (2016b) provisions:

$$M_{cr} = \frac{C_b S_{xc} \pi^2 E}{\left(K_e L_b / r_t\right)^2} \sqrt{1 + 0.078 \frac{J}{S_{xc} h_o} \left(\frac{K_e L_b}{r_t}\right)^2} \qquad (2)$$

An expedient process to determine K_e is to employ the goal-seek root-finding capability in Excel to iteratively solve for the value of K_e that satisfies the equality.

In Equation 2, C_b is the moment gradient factor, E is the elastic modulus, S_{xc} is the section modulus, L_b is the unbraced length of the critical section, r_t is the radius of gyration for LTB, J is the St. Venant torsion constant, and h_o is the distance between the flange centroids. For the slender-web members, J was taken equal to zero in Equation 2, as well as in the calculation of the buckling load from SABRE2. The calculated value of K_e is used in all recommended and AISC *Specification* strength calculations of this research to directly account for the end restraint from adjacent less-critical unbraced lengths due to continuity effects. An alternative means of calculating K_e is to use an approximate method such as that proposed by Nethercot and Trahair (1976). However, with the increased availability of software capable of conducting basic elastic linear buckling analysis (ELBA), the "exact" calculation of K_e is the more appropriate solution for research evaluations.

ABAQUS Version 6.13 (Simulia, 2021) finite element analysis software was employed for developing GMNIA (geometric nonlinear material linear-elastic analysis with imperfections) finite element simulations in this research. The finite element mesh consisted of B31 beam elements for transverse stiffeners and S4R nonlinear shell elements for all other components. The B31 is a two-node, three-dimensional beam element that allows for transverse shear deformation. The B31 element is based on linear-order displacement interpolation and is compatible with the S4R shell element. The S4R is a four-node, quadrilateral displacement-based shell element with reduced integration. Both the B31 and the S4R elements are based on large-strain formulations. The shell finite element mesh for the I-section specimens was generated using 12 elements across the flange width and a minimum of 16 elements through the web depth. The dimension of the shell elements along the length of the members was selected such that the aspect ratio of the web elements was close to 1.0. This mesh density has been determined to be sufficient for convergence of full nonlinear FEA solutions of various I-section members in prior research—for example, Prado and White (2015)—as well as in these research studies.

The nonlinear shell FEA solutions in ABAQUS were implemented through a modified RIKS arc length procedure. The modified RIKS algorithm is particularly useful in obtaining the post-buckling response for cases where the loading is proportional—that is, where the load magnitudes are governed by a single parameter (Simulia, 2021). The modified RIKS algorithm conducts a load-deflection analysis where the load is incremented by scaling the reference load, or a set of applied reference loads, by the load parameter. The definition of initial residual stresses, and the application of the applied loads to the test specimens starting from their loaded state under their self-weight, was accomplished by subdividing the analysis into multiple steps. Note that the residual stress pattern follows half the magnitude of the best-fit Prawel pattern based on recommendations from Subramanian and White (2017), who state that this provides reasonable correlation with the mean results from experimental tests. A first step was employed to solve for the equilibration of the initial residual stresses on the geometrically imperfect model (the initial residual stress pattern generally does not satisfy equilibrium on the imperfect structure geometry, nor at free-ends of the specimens). A second step was then employed to apply the constant self-weight loads. Finally, the modified RIKS algorithm was applied in a third step to place the applied load incrementally on the model.

VALIDATION OF THE TEST SETUP THROUGH AN ELASTIC LTB TEST

A benchmark elastic LTB experiment was conducted to evaluate the effectiveness of the translation and rotational releases in the test setup. Figure 1 provides an elevation view of the test specimen as well as the moment diagram. The elevation view and measured section dimensions in Figure 1 is drawn to scale and shows instrumentation locations. For the critical unbraced lengths adjacent to the mid-span, C_b = 1.38 from AISC *Specification* Commentary Equation C-F1-2b (AISC, 2016b) and K_e = 0.82 for the critical unbraced lengths adjacent to the mid-span (back-calculated from an elastic buckling analysis conducted using SABRE2). The resulting configuration slenderness was well within the elastic LTB range.

It is important to note that due to stable elastic post-buckling response in the governing LTB mode, the specimen potentially can develop a maximum load capacity larger than the elastic critical load, due to the large LTB

slenderness for the elastic LTB testing arrangements. Any actual post-buckling strength is directly dependent upon the extent of early yielding due to the combined effects of the girder loads, the initial geometric imperfections, the initial residual stresses, and the amplified lateral bending of the compression flange as the theoretical elastic critical load is approached. The peak load at which the elastic LTB test reached is compared directly to the theoretical elastic LTB resistance and to the capacity predicted from shell FEA test simulation. The FEA simulation models included the evaluation of the post-peak response. Additionally, plots of the horizontal displacement of the flanges versus the load were employed to estimate the theoretical elastic LTB moments via Southwell, Meck, and Massey plots (Mandal and Calladine, 2002).

The test specimen was fabricated by a prominent metal building manufacturer and is representative of main frame members in typical metal building frames. The web-to-flange welds are minimum size single-sided fillet welds. Both flanges are fabricated from rolled bar stock, while the web was cut from a coil. In addition, the specimen has double-sided stiffener plates at all the brace points, including load and bearing locations, to control cross-sectional distortion.

Measured compression flange sweep and web out-of-flatness of the test specimen are shown in Figures 8 and 9, respectively. Geometric imperfection measurements were taken after the beam was installed and plumbed. Allowable tolerances of $L_b/480$ for compression flange sweep and $h/72$ for web out-of-flatness are specified in the *Metal Building*

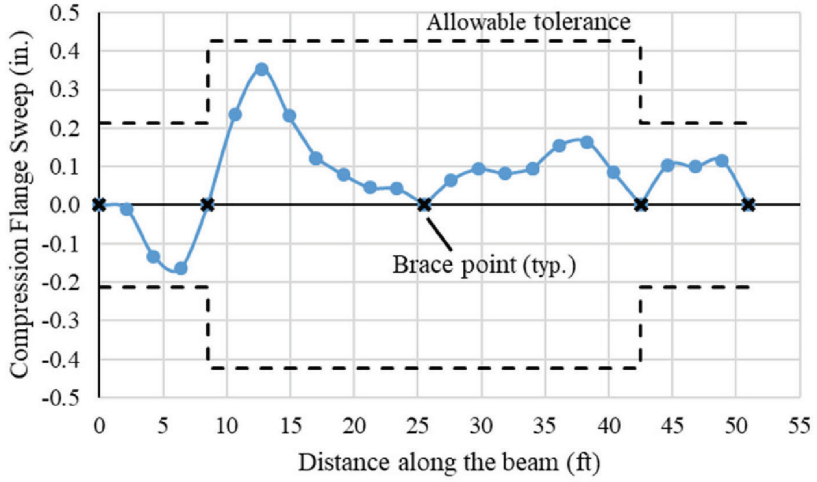

Fig. 8. Measured compression flange sweep.

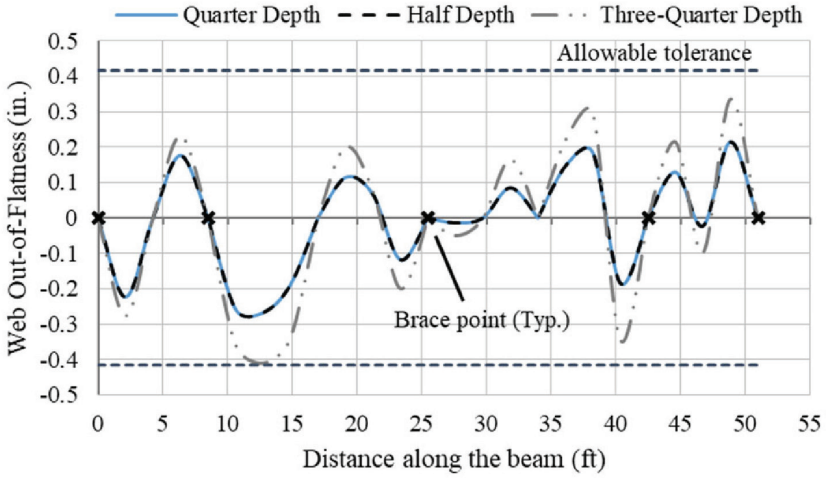

Fig. 9. Measured web out-of-flatness.

Table 1. Peak Moment Contributions		
Maximum Moment at Mid-Span Due to Dead Loads		
Dead Load	**Calculation**	**Moment kip-ft (kip-in.)**
Girder self-weight	(0.036 klf) (51 ft)^2/8	11.6 (139)
Mid-span attachments	(0.38 kip) (51 ft)/4	4.95 (59.4)
Bracing attachments	(0.07 kip) (8 ft)	0.540 (6.50)
Maximum Moment at Mid-Span Due to Applied Loads		
Applied Load	**Calculation**	**Moment kip-ft (kip-in.)**
Initial seating preload	(0.50 kip) (51 ft)/4	6.38 (76.5)
Actuator load at failure	(8.51 kips) (51 ft)/4	109 (1300)
	Maximum moment at mid-span	133 (1600)

Systems Manual (MBMA, 2018). These tolerances are approximately double the imperfection limits given by the AISC *Code of Standard Practice* (AISC, 2016a). The other measured imperfections—that is, tension flange sweep, combined flange warpage and tilt, and web off-center—were documented but are not specified in this paper. A detailed force and moment tabulation is summarized in Table 1, including the influence of all self-weights of the testing specimen and bracing components, load applied prior to zeroing the load cells at the start of the experiment, and the measured peak load during the experiment.

The experimental strength of 1,600 kip-in. is normalized by the moment corresponding to compression flange yielding, M_{yc}, of 4,760 kip-in. and plotted in Figure 10 at the effective length, K_eL_b = 13.9 ft. Furthermore, Figure 10 shows numerical strength predictions from an ABAQUS nonlinear shell FEA test simulation and from a thin-walled open-section (TWOS) beam theory inelastic buckling analysis using SABRE2, as well as estimates of the theoretical elastic buckling load from a Southwell plot based on the measured experimental displacements.

In addition, Figure 10 shows the normalized theoretical elastic buckling curve from Equation 2 for a range of members having the same configuration as in Figure 1 but with different effective unbraced lengths, using the calculated finite J for the specific specimen. This is the dashed black curve in the figure. Also shown in light gray is the LTB strength curve from the recommended provisions presented in Slein et al. (2021). This curve is based on $J = 0$ since the web for this cross section classifies as slender using

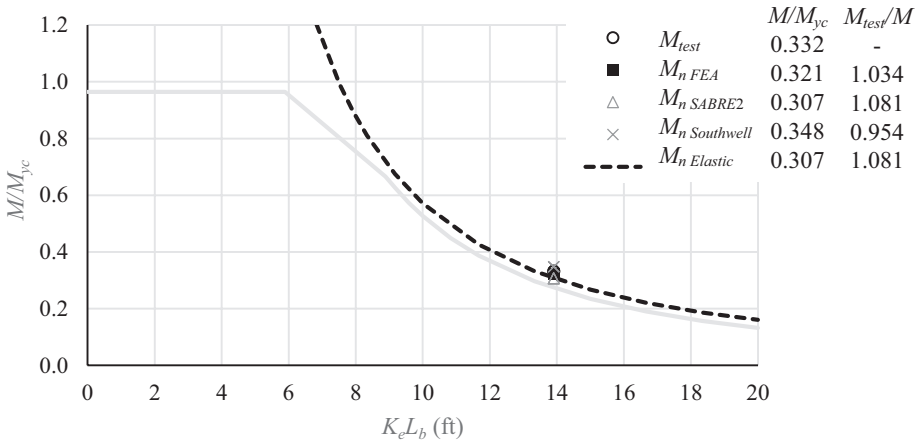

Fig. 10. Comparison of experimental test results to numerical results from ABAQUS and SABRE2 to a Southwell plot estimate of the elastic buckling load and to elastic LTB and design strength curves.

the recommended provisions. The "exact" elastic critical moment for the specimen is determined using SABRE2, and the K_e value is determined using Equation 2 (using the solution based on $J = 0$ for this member because its web is classified as slender in the recommended provisions).

Figure 11 shows the measured moment versus vertical displacement for SP-2, overlaying the predicted moment-maximum vertical displacement from the shell FEA. Figure 12 shows the measured moment versus lateral displacements for SP-7 and SP-8, overlaying the predicted moment-maximum horizontal displacement of the compression flange and the corresponding horizontal displacement of the tension flange from the shell FEA. Figure 13 shows the measured moment versus section twist at the cross section where SP-7 and SP-8 are attached, overlaying the predicted moment-twist from the shell FEA.

The GMNIA solution from ABAQUS is capable of capturing a capacity in the elastic test that is larger than the theoretical elastic LTB strength due to the stable elastic post-buckling response of the member. The contributions from elastic post-buckling strength are negligible for most practical LTB slenderness values; however, given the large slenderness in this elastic LTB test, strengths larger than the theoretical elastic LTB resistance are possible. Figure 14 shows the midspan moment versus the compression flange lateral deflection from the GMNIA solution, a shell

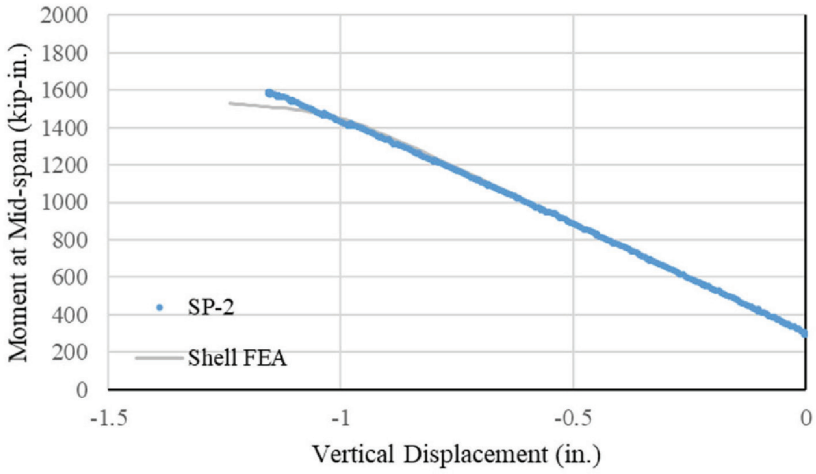

Fig. 11. Moment-vertical deflection.

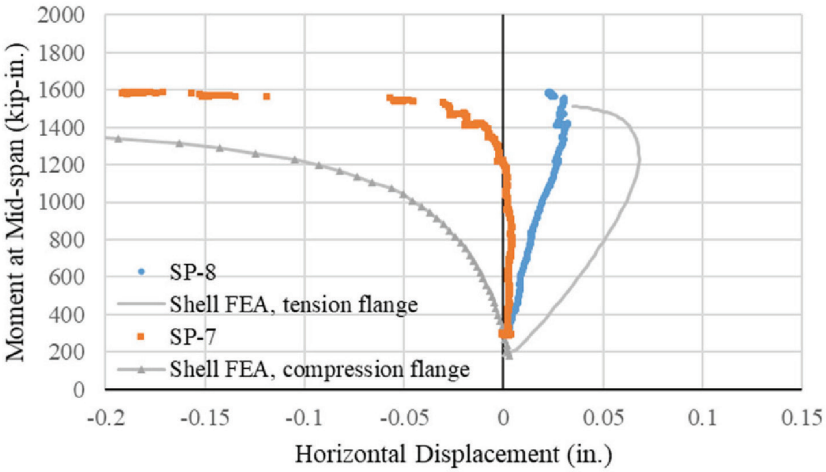

Fig. 12. Moment-horizontal deflection of both flanges.

FEA geometric nonlinear (material linear-elastic) analysis with imperfections using the same model as in the GMNIA solution (referred to in the literature as a GNIA solution), and the ELBA solution obtained from SABRE2.

As the theoretical elastic critical moment is approached, the compression flange lateral displacement increases rapidly, both in the full nonlinear (GMNIA) and the geometrically nonlinear (GNIA) shell FEA solutions. The corresponding rapid increase in the compression flange lateral bending strains induces the onset of yielding within the compression flange, resulting in a limit load in the GMNIA solution. This behavior was observed during the experiment, that when the rate of change of the compression flange lateral displacements increases abruptly, the member was very close to maximum capacity. The second-order amplifications of the girder lateral displacements and twists in the experiment matched well with the theory.

Experimental Estimation of Elastic Buckling Load by Southwell, Meck, and Massey Plots

As a final evaluation of the test setup effectiveness—specifically the minimization of incidental restraint—measured displacements and loads were used to generate Southwell, Meck, and Massey plots for the elastic tests. These plots allow estimation of the elastic critical moment

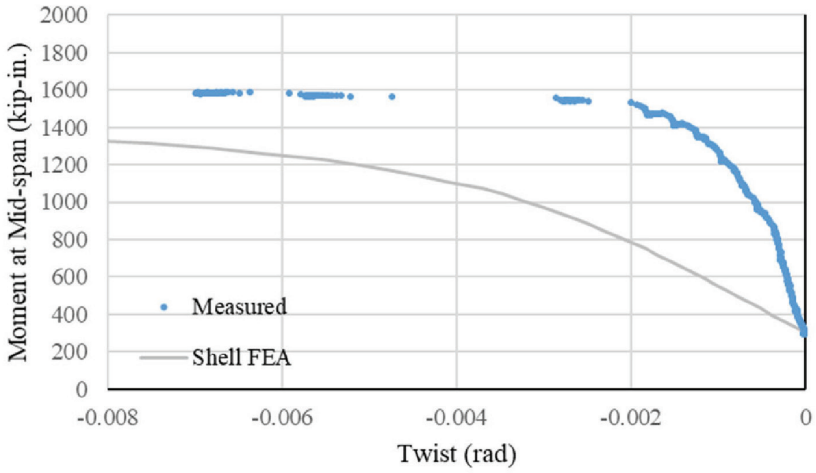

Fig. 13. Moment-twist of the section.

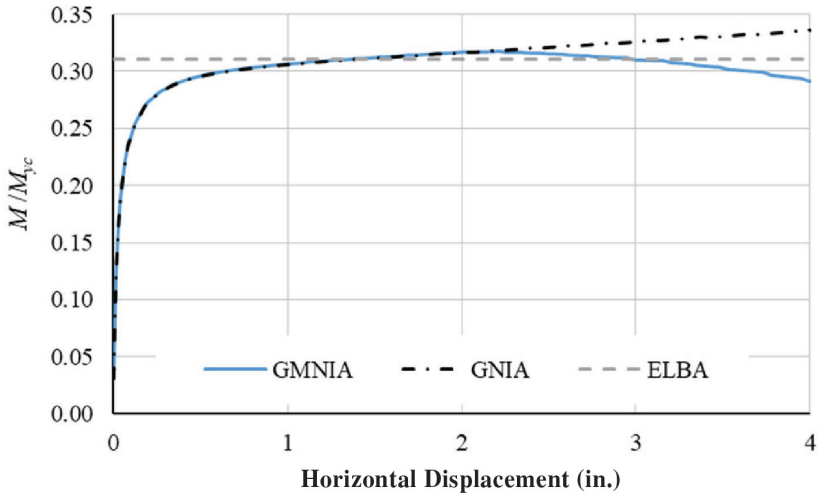

Fig. 14. Load-horizontal displacement curves from ABAQUS GMNIA and GNIA solutions compared to the ELBA solution from SABRE2.

of the specimen, M_{cr}. Mandal and Calladine (2002) discuss the effectiveness and theoretical underpinnings of these plots for LTB problems. Each of the methods plot a variation of a displacement divided by a load term versus displacement, then use the inverse of the slope of this curve to estimate M_{cr}. The authors interpreted the application of the different estimation methods as described in the following discussion.

The Southwell plot for LTB was generated using the lateral displacement of the compression flange, u, as the abscissa versus u/M as the ordinate. The lateral displacement was measured using a linear string potentiometer, located at the expected position of the maximum compression flange lateral displacement. The estimate is not sensitive to the specific selected location as long as the magnitude of the instrumentation noise is low compared to the magnitude of the measurement. The maximum moment at mid-span was calculated as

$$M = \frac{PL}{4} + M_o \tag{4}$$

where P is the summation of load cell measurements at the end supports, L is the distance between the end supports, and M_o is the mid-span dead load moment. Figure 15 shows the resulting Southwell plot for the elastic test.

The Meck plot was similar to the Southwell plot, but it also considers the twist of the cross section, φ. During the elastic test the tension flange had negligible out-of-plane motion, as shown in Figure 12; therefore, the twist of the cross section is directly proportional to the lateral displacement of the compression flange. The Meck plot takes M_{cr} as the square root of the product of α (the inverse slope of φ/M versus u) and β (the inverse slope of u/M versus φ)—that is, the geometric mean of α and β,

$$M_{cr} = \sqrt{\alpha\beta} \tag{5}$$

The Massey plot takes M_{cr} as the geometric mean of α (taken as the inverse slope of φ/M^2 versus φ), and β (taken as the inverse slope of u/M^2 versus u). The values of α and β for the Meck and Massey plots are defined by the slope of the corresponding plots, similar to M_{cr} on the Southwell plot. There is some complexity that is not captured by these methods since the critical unbraced lengths of the specimen are not flexurally and torsionally simply supported. As such, the second-order amplifications of the compression flange lateral deflection, u, and the twist, φ, do not have the same mathematical form as that of a simply supported column (for that matter, they do not have the same form when the LTB specimen is torsionally and simply supported, which leads to the consideration of the alternative estimation procedures other than the basic Southwell plot). However, the methods agree reasonably well with each other for the elastic test. In the limit that the moment approaches the theoretical elastic buckling moment, it appears that the simple assumptions for the form of the second-order amplification of the displacements, embedded within the Southwell, Meck, and Massey plots, apply reasonably well. The calculated maximum moments are 1,660 kip-in. ($0.348M_{yc}$), 1,640 kip-in. ($0.344M_{yc}$), and 1,570 kip-in. ($0.329M_{yc}$) from the Southwell, Meck, and Massey procedures, respectively. These theoretical estimates show good agreement with the maximum moment of 1,600 kip-in. measured in the experiment.

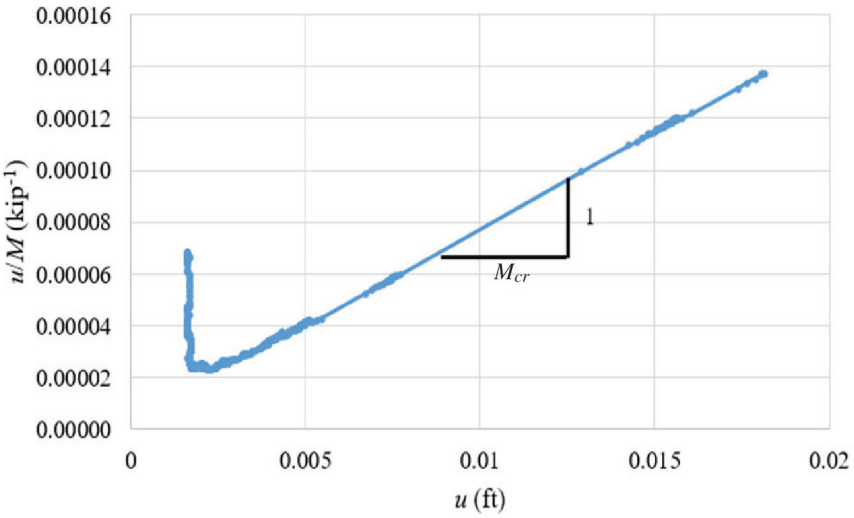

Fig. 15. Southwell plot.

QUANTIFICATION OF INCIDENTAL RESTRAINT

To quantify the ability of the testing system to minimize incidental restraint, the buckling load solutions from Southwell, Meck, and Massey are compared with the result from an elastic linear buckling analysis (ELBA). The effective length in the theoretical elastic buckling solution is back-calculated directly from an ELBA in SABRE2, so the theoretical elastic buckling solution from Equation 2 and the SABRE2 ELBA are the same. The reported SABRE2 solutions are from an inelastic nonlinear buckling analysis (INBA). Note that K_eL_b in the elastic test is much larger than L_r; therefore, the major-axis bending moment is at a level where there is not a significant onset of yielding prior to reaching the maximum capacity, resulting in a similar INBA solution as ELBA. Structural steels such as ASTM A572 Grade 55 generally have a mean elastic modulus close to 29,500 ksi with a small coefficient of variation (Hartmann, 2005). Using this larger elastic modulus in the ELBA solution gives a more accurate representation of the physical response. The elastic critical moment scales by 29,500/29,000 given this change.

For the elastic test, the Southwell, Meck, and Massey estimates give M_{cr}/M_{yc} ranging from 0.329 to 0.348. The ELBA eigenvalue result from SABRE2, with E = 29,500 ksi, gives M_{cr}/M_{yc} of 0.312. Therefore, in terms of elastic buckling load, the test shows an influence of incidental constraint of 5 to 12%, depending on which estimates are used for determining the elastic critical moment experimentally.

To a lesser extent, the ability of the testing system to minimize incidental restraint can be quantified by comparing the experimental load to the shell FEA load-deflection solution. The M_{test}/M_{nFEA} value was 1.03 for the elastic test. However, the elastic test was halted prior to reaching the limit load (when the compression flange lateral bending started to increase significantly) to ensure that no significant yielding occurred, since the specimen is subsequently used for an inelastic LTB test, resulting in slightly low measured experimental strengths. This is more of a problem when KL_b is in the proximity to L_r, due to the greater propensity for the onset of yielding due to the addition of amplified flange lateral bending stresses as the theoretical elastic buckling load was approached. Additionally, potential overprediction of M_{nFEA} can be a source of error. The shell FEA test simulation potentially could have overpredicted the strength, for example, by its use of one-half of the best-fit Prawel residual stress profile (i.e., by assuming residual stresses that are relatively small and symmetric about the mid-width of the flanges), as well as by excluding the web off-center imperfections in the modeling of the specimen geometry, in this test. The maximum strength obtained in the FEA solution can be sensitive to variations in the residual stresses and geometric imperfections when the compression flange major-axis bending stress is relatively large at the LTB strength condition. The expected sensitivities of M_{test} and M_{nFEA} to the residual stresses and geometric imperfections when KL_b is close to L_r, and the uncertainties in the precise values of these quantities, makes the use of M_{test}/M_{nFEA} less of a useful measure of incidental constraint within the testing system.

CONCLUSIONS

Incidental restraint can have a measurable impact on experimental LTB test results. Substantial attention was given to minimizing the constraint in the experimental setup described in this paper. The setup design consists of ideally released degrees of freedom, while restraining specified degrees of freedom, using mechanical bearings in a Watt's linkage bracing system. PTFE spherical thrust bearing allowed for free flange lateral bending and major-axis and weak-axis rotation. Complications of load height were bypassed with placing stiffeners at points of load application and bearing, along with a lateral brace of both flanges. For an accurate comparison to strength predictions, numerical solutions were modeled to be representative of the physical specimen and manual predictions utilized a rigorously calculated effective length factor.

To validate the effectiveness of the testing setup, an elastic LTB test was conducted and compared to analytical and numerical predictions, as well as to theoretical elastic critical moment estimates. The most direct prediction of the effectiveness of the setup is believed to be the comparison of the buckling load solutions from Southwell, Meck, and Massey to an elastic linear buckling analysis. Resulting data indicated an influence from incidental restraint on the LTB strength ranging between 5 and 12%, depending on the methodology. The nominal difference can be attributed to the small amount of remaining restraint as well as other factors influencing the predictions, such as discrete measurements of plate dimensions, material properties, and geometric imperfections. Ultimately, the results demonstrate the designed test configuration minimizes incidental constraint, resulting in accurate experimental LTB test data.

ACKNOWLEDGMENTS

The authors would like to acknowledge MBMA, AISC, and AISI for their generous support of this research; American Buildings Company, BlueScope Buildings North America, and Schulte Building Systems for their generous donations

of the test specimens; AISC and NUCOR Fastener Division for material and fastener donations; and Thomas Murray of Virginia Tech for acting as the MBMA senior advisor to the project. They would also like to thank the Georgia Tech Structural Engineering Laboratory staff and other GT personnel for their many contributions to the project.

REFERENCES

AASHTO (2020), *AASHTO LRFD Bridge Design Specifications*, 8th Ed., American Association of State and Highway Transportation Officials, Washington, D.C.

AISC (2005), *Specification for Structural Steel Buildings*, ANSI/AISC 360-05, American Institute of Steel Construction, Chicago, Ill.

AISC (2016a), *Code of Standard Practice for Steel Buildings and Bridges*, ANSI/AISC 303-16, American Institute of Steel Construction, Chicago, Ill.

AISC (2016b), *Specification for Structural Steel Buildings*, ANSI/AISC 360-16, American Institute of Steel Construction, Chicago, Ill.

Hartmann, J.L. (2005), "An Experimental Investigation of the Flexural Resistance of Horizontally Curved Steel I-Girder Systems," Doctoral Dissertation, University of Maryland, College Park, Md.

Lindapter (2019), *Steel Connections Catalog*, Lindapter USA, http://www.lindapter.com/ (April 22).

Mandal, P. and Calladine, C.R. (2002), "Lateral-Torsional Buckling of Beams and the Southwell Plot," *International Journal of Mechanical Sciences*, Vol. 44, No. 12, pp. 2,557–2,571.

MBMA (2018), *Metal Building Systems Manual*, Metal Building Manufacturers Association, Cleveland, Ohio.

McGuire, W., Gallagher, R., and Ziemian, R.D. (2000), *Matrix Structural Analysis*, 2nd Ed., Wiley, New York, N.Y.

Nethercot, D.A. and Trahair, N.S. (1976), "Lateral Buckling Approximations for Elastic Beams," *Structural Engineering*, Vol. 54, No. 6, pp. 197–204.

Prado, E.P. and White, D.W. (2015), "Assessment of Basic Steel I-Section Beam Bracing Requirements by Test Simulation," Structural Engineering, Mechanics and Materials Report, School of Civil and Environmental Engineering, Georgia Institute of Technology, Atlanta, Ga.

Simulia (2021), Abaqus 6.13, Dassault Systems, https://www.3ds.com/products-services/simulia/services-support/support/documentation/ (February 22).

Slein, R., Kamath, A.M., Latif, W., Phillips, M.L., Sherman, R.J., Scott, D.W., and White, D.W. (2021), "Enhanced Characterization of the Flexural Resistance of Built-up I-Section Members," SEMM Research Report 21-01, School of Civil and Environmental Engineering, Georgia Institute of Technology, Atlanta, Ga.

Smith, M.D., Turner, A.K., and Uang, C.-M. (2013), "Experimental Study of Cyclic Lateral-Torsional Buckling of Web-Tapered I-Beams," Department of Structural Engineering University of California, San Diego, Calif.

Subramanian, L., Jeong, W.Y., Yellepeddi, R., and White, D.W. (2018), "Assessment of I-Section Member LTB Resistances Considering Experimental Tests and Practical Inelastic Buckling Design Calculations," *Engineering Journal,* AISC, Vol. 55, No. 1, pp. 15–44.

Subramanian, L. and White, D.W. (2017), "Resolving the Disconnect between Lateral Torsional Buckling Experimental Tests, Test Simulations and Design Strength Equations," *Journal of Constructional Steel Research*, Vol. 128, pp. 321–334.

Toğay, O. and White, D.W. (2018), "Toward the Recognition of Unaccounted for Flange Local Buckling and Tension Flange Yielding Resistances in the ANSI/AISC 360 Specification," *Proceedings of the SSRC Annual Stability Conference*, Baltimore, Md.

White, D.W., Toğay, O., Slein, R., and Jeong, W.Y. (2020), "SABRE2-V2," white.ce.gatech.edu/sabre (January 17).

Yarimci, E., Yura, J.A., and Lu, L.W. (1967), "Techniques for Testing Structures Permitted to Sway," *Experimental Mechanics*, Vol. 7, No. 8, Reprint, Fritz Laboratory Reports, Paper 112, http://preserve.lehigh.edu/engr-civil-environmental-fritz-lab-reports/112.

Ziemian, R.D. (Ed.) (2010), *Guide to Stability Design Criteria for Metal Structures*, 6th Ed., John Wiley & Sons, Inc., Hoboken, N.J.